VNU Journal of Science: Mathematics - Physics

Journal homepage: https://js.vnu.edu.vn/MaP

Original Article

Synthesis and Characterization of $ZnO/NiFe_2O_4$ Materials

Tran Thi Viet Nga[1,*], Tong Minh Thang[2], To Thanh Loan[1], Nguyen Thanh Phuong[2]

[1]*School of Materials Science and Engineering, Hanoi University of Science and Technology, 1 Dai Co Viet, Hanoi, Vietnam*

[2]*Faculty of Engineering Physics, Hanoi University of Science and Technology, 1 Dai Co Viet, Hanoi, Vietnam*

Received 6th January 2026
Revised 19th March 2026; Accepted 28th April 2026

Abstract: This study reports the synthesis and characterization of $ZnO/NiFe_2O_4$ nanocomposites for potential application in photocatalytic wastewater treatment. The composites were prepared via a two-step hydrothermal process with Zn^{2+}/Ni^{2+} molar ratios of 1, 1.5, and 2. X-ray diffraction combined with Rietveld refinement confirmed the coexistence of characteristic crystalline phases with nanoscale particle sizes. SEM observations revealed distinct morphologies. Magnetic characterization using a vibrating sample magnetometer indicated that pure $NiFe_2O_4$ exhibited soft magnetic behavior, while the saturation magnetization of the composites decreased as ZnO content increased. UV–Vis spectroscopy and band gap analysis demonstrated an extension of optical absorption from the ultraviolet to the visible region. These properties suggest that $ZnO/NiFe_2O_4$ composites may serve as potential candidates for magnetically recoverable photocatalysts, although photocatalytic performance evaluation will be the subject of future work.

Keywords: $ZnO/NiFe_2O_4$, composite materials, photocatalysis.

1. Introduction

Water pollution, particularly from industrial effluents containing persistent organic pollutants such as synthetic dyes, has emerged as a critical threat to environmental sustainability and public health. Conventional treatment technologies often suffer from limited efficiency and high operational costs, thereby necessitating alternative strategies. Among these, photocatalytic oxidation employing semiconductor-based materials to drive redox reactions under light irradiation has gained considerable attention as a green, cost-effective, and highly efficient approach [1].

* Corresponding author.
E-mail address: nga.tranthiviet@hust.edu.vn

https//doi.org/10.25073/2588-1124/vnumap.5106

A wide range of photocatalytic materials has been extensively explored, among which zinc oxide (ZnO) has attracted considerable attention owing to its low cost, non-toxicity, and high optical absorption efficiency relative to many alternatives [2]. Nevertheless, the photocatalytic efficiency of ZnO remains severely constrained under visible-light irradiation, primarily due to its wide band gap (3.37 eV) and the rapid recombination of photogenerated electron–hole pairs, which collectively hinder its catalytic performance. Furthermore, ZnO is prone to photocorrosion during prolonged operation, further limiting its practical applicability [3-5]. Conversely, nickel ferrite ($NiFe_2O_4$) has emerged as a promising candidate because of its intrinsic magnetic properties, excellent thermal stability, and relatively narrow band gap (~1.7 eV), which facilitates strong visible-light absorption. However, its overall photocatalytic activity is impeded by the intrinsically low efficiency of electron–hole pair generation, thereby restricting its practical performance [6, 7].

The integration of these two semiconductors provides a synergistic strategy to exploit their complementary properties, thereby enhancing light-harvesting capability and improving overall photocatalytic efficiency for wastewater remediation. Moreover, the intrinsic magnetic behavior of $NiFe_2O_4$ enables facile separation and recovery of the catalyst after the reaction, further contributing to its practical applicability in sustainable water treatment systems.

2. Experiments

2.1. Sample Preparation

The $ZnO/NiFe_2O_4$ nanocomposites were synthesized through a two-step hydrothermal approach. In the first step, $NiFe_2O_4$ nanoparticles were prepared via a controlled hydrothermal process. In the subsequent step, ZnO was hydrothermally grown in the presence of the pre-formed $NiFe_2O_4$ nanoparticles.

2.1.1. Synthesis of $NiFe_2O_4$ Nanoparticles

$NiFe_2O_4$ nanoparticles were synthesized via a hydrothermal method. Briefly, 2.5 mL of $Ni(NO_3)_2$ 1 M and 5 mL of $Fe(NO_3)_3$ 1 M were dissolved in 40 mL of deionized water under continuous stirring. Subsequently, 1.5 mL of PEG-400 was added as a dispersing agent, and the solution was stirred for 30 min. A NaOH 1 M solution was then added dropwise under vigorous stirring until the pH reached ~12. The resulting suspension was stirred for another 30 min, transferred into a Teflon-lined stainless-steel autoclave, and heated at 180 °C for 5h. After cooling to room temperature, the precipitate was collected by filtration, washed repeatedly with deionized water, and dried at 60 °C for 24h to obtain $NiFe_2O_4$ nanoparticles.

2.1.2. Synthesis of $ZnO/NiFe_2O_4$ Nanocomposites

The synthesis of $ZnO/NiFe_2O_4$ was carried out using precursor salt solutions. Specifically, 2.5 mL of $Ni(NO_3)_2$, 2.5 mL of $Zn(NO_3)_2$, 5 mL of $Fe(NO_3)_3$, and 40 mL of deionized water were mixed in a beaker and magnetically stirred for 15 min to obtain a homogeneous solution. Subsequently, 2 mL of PEG-400 was added to the mixture and stirred for 30 min to control particle dispersion. A 1 M NaOH solution was then slowly added dropwise under vigorous stirring until the pH of the solution reached approximately 12. The resulting suspension was further stirred for 1 h and ultrasonicated for an additional 1h. The mixture was then subjected to hydrothermal treatment at 180 °C for 6h. After completion of the reaction, the obtained product was filtered, washed, and dried at 60 °C for 24h, yielding $ZnO/NiFe_2O_4$ nanoparticles.

A series of samples (denoted as M) were prepared with different Zn^{2+}/Ni^{2+} molar ratios, as summarized in Table 1.

Table 1. Zn^{2+}/Ni^{2+} ratios of the M series samples.

Sample	NFO	ZnO	M-1	M-1,5	M-2
Zn^{2+}/Ni^{2+}	0/1	1/0	1/1	1.5/1	2/1

2.1. Characterization Techniques

The crystal structure and phase composition of the samples were characterized by X-ray diffraction (XRD), and the diffraction patterns were refined using the Rietveld method implemented in the FullProf software. A Voigt function, combining Gaussian and Lorentzian components, was used to model the diffraction peaks. The refinement quality was evaluated based on the χ^2 and R_{wp} values, with ideal thresholds of $\chi^2 \approx 1$ and Rwp < 10%. The morphology and particle size were analyzed using scanning electron microscopy (SEM), while magnetic properties were measured with a vibrating sample magnetometer (VSM) under an applied field of –15 to +15 kOe. The optical properties were examined by ultraviolet–visible (UV–Vis) spectroscopy.

3. Results and Discussion

3.1. Crystal Structure and Morphological Characteristics

Figure 1 presents the X-ray diffraction (XRD) patterns of the M-series samples refined by the Rietveld method, with the corresponding Rwp and χ^2 values summarized in Table 2. The NFO sample exhibits a cubic spinel structure (space group Fd-3m), characteristic of the $NiFe_2O_4$ phase. In general, reliable refinements are often associated with Rwp values below 10%. However, in multiphase nanocrystalline systems with broadened diffraction peaks and minor secondary phases, slightly higher Rwp values may occur. In the present case, the obtained Rwp values (approximately 14–17%) together with χ^2 values close to unity and randomly distributed difference curves indicate that the refinements remain reliable for phase identification and semi-quantitative analysis. All observed Bragg reflections can be indexed to the $NiFe_2O_4$ phase, with no detectable secondary phases, thereby demonstrating the formation of a single-phase spinel structure with high purity.

The occurrence of overlapping Bragg reflections can be attributed to the use of an XRD instrument equipped with an X-ray source that emits two characteristic wavelengths, $K\alpha_1$ and $K\alpha_2$. Specifically, Cu-Kα radiation (or a comparable source) consists of two main components: $K\alpha_1$ with a shorter wavelength ($\lambda_1 \approx 1.5406$ Å for Cu) and $K\alpha_2$ with a slightly longer wavelength ($\lambda_2 \approx 1.5444$ Å for Cu). For the ZnO sample, the experimental diffraction profile shows excellent agreement with the calculated model, as evidenced by the overlap of the two patterns and the random distribution of the difference curve around the baseline. All Bragg reflections were indexed to the ZnO phase, with no detectable secondary phases, thereby confirming the formation of a single-phase ZnO material with high purity.

For all three M-series samples, the calculated diffraction pattern (I^{cal}) shows good agreement with the experimental data (I^{obs}), and the difference curve ($I^{obs} - I^{cal}$) is randomly distributed around the baseline. The Bragg reflection markers indicate the positions of the diffraction peaks corresponding to each phase present in the materials, including $NiFe_2O_4$, ZnO, and β-$Ni(OH)_2$ in all samples. A very small amount of α-Fe_2O_3 phase was suggested by the Rietveld refinement (below ~3 wt%). Due to its extremely low fraction and peak overlap with the main phases, the diffraction peaks are not clearly distinguishable and therefore this phase should be considered as a minor possible impurity rather than a definitively confirmed phase. The presence of β-$Ni(OH)_2$ is supported by weak diffraction reflections that can be indexed to its characteristic planes, such as (101) and (102). The formation of this phase may

originate from incomplete conversion of Ni^{2+} species under strongly alkaline hydrothermal conditions (pH ≈ 12).

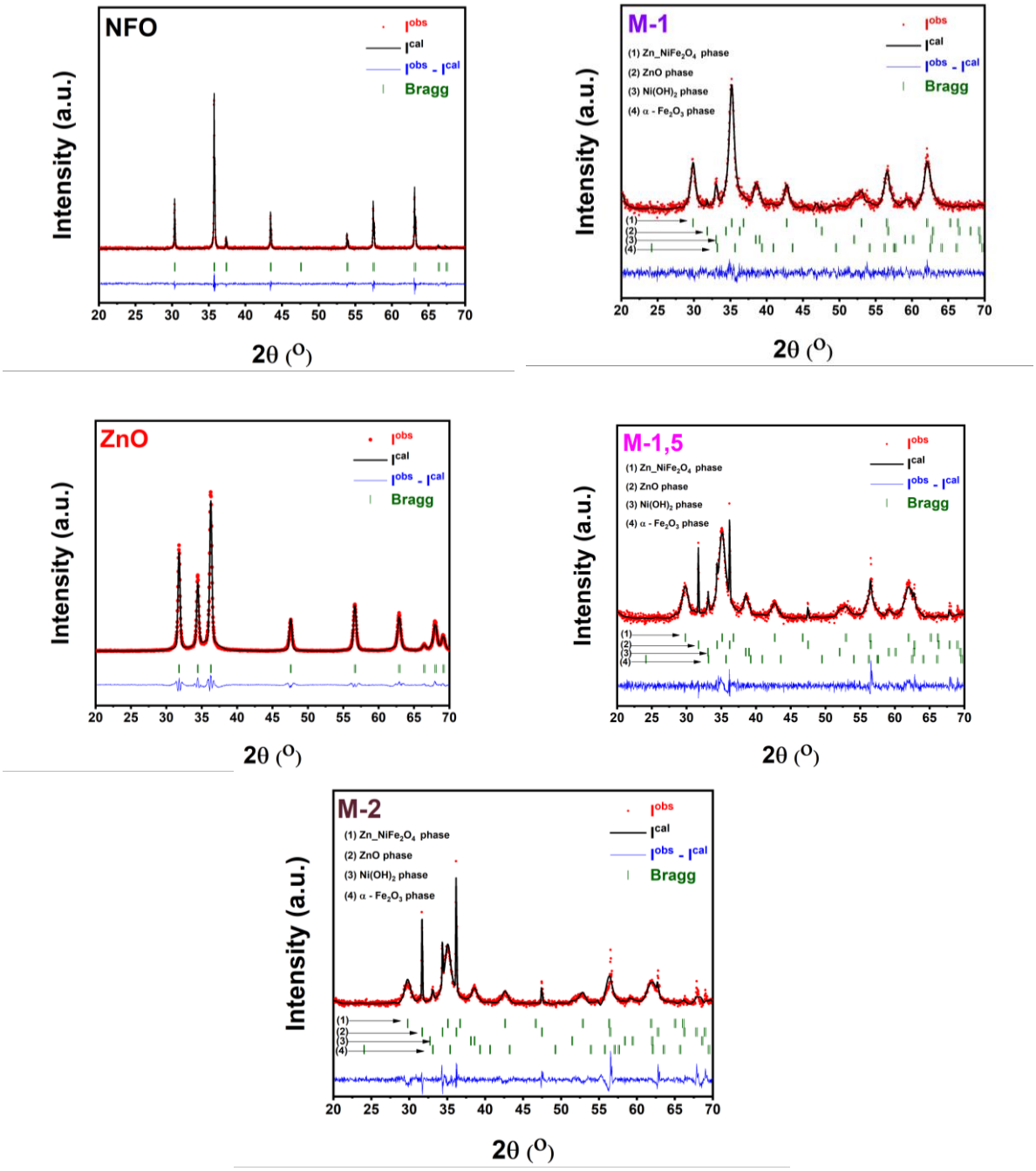

Figure 1. Rietveld refinement results of the M series samples.

The X-ray diffraction (XRD) patterns of the M-1, M-1,5, and M-2 samples, as shown in Figure 2, reveal the formation of three main crystalline phases: spinel $Ni(Zn)Fe_2O_4$, ZnO with a wurtzite structure,

and β-Ni(OH)$_2$. For the M-1 sample with a molar ratio of Ni:Zn:Fe = 1:1:2, the diffraction peaks characteristic of the spinel phase, such as (220), (311), (400), (511), and (440), are observed with high intensity. In this sample, the β-Ni(OH)$_2$ phase is clearly identified by the reflections from the (101) and (102) planes, whereas the diffraction peaks corresponding to ZnO are nearly absent. When the Zn content is increased to 1.5 in the M-1,5 sample, several characteristic ZnO peaks emerge at 2θ = 31.8°, 36.2°, 47.5°, 56.6°, and 68°, indicating that excess Zn^{2+} ions that do not participate in the spinel structure crystallize into the ZnO phase. For the M-2 sample, which contains the highest excess of Zn^{2+}, the pronounced appearance of ZnO and β-Ni(OH)$_2$ peaks, together with the relative decrease in the intensity of spinel reflections compared to those of ZnO, suggests the saturation of Zn^{2+} and Ni^{2+} incorporation into the spinel lattice. This observation indicates that when the amounts of Zn^{2+} and Ni^{2+} exceed their ability to react with Fe^{3+} to form the spinel phase, the excess ions segregate and crystallize as separate ZnO and β-Ni(OH)$_2$ phases.

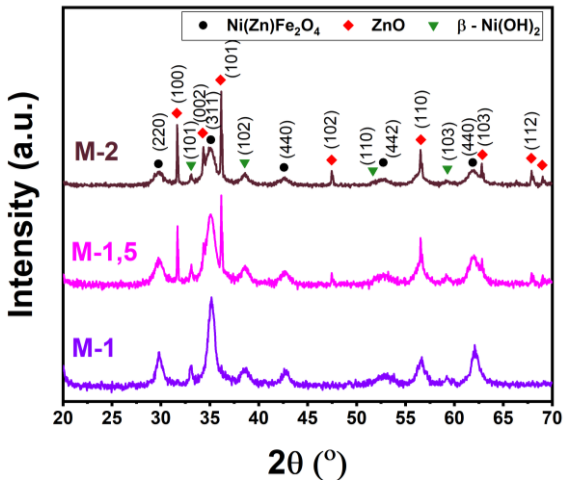

Figure 2. X-ray diffraction patterns of the M-1, M-1,5, and M-2 samples.

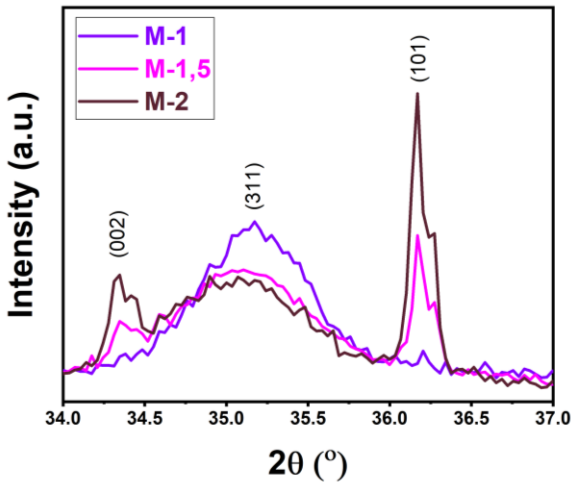

Figure 3. X-ray diffraction patterns of the M-1, M-1,5, and M-2 samples in the 2θ range from 34° to 37°.

The emergence of these secondary phases can be attributed to the molar ratio of the supplied metal ions, Ni:Zn:Fe = 1:1:2 (M-1 sample), which is lower than the Fe:M = 2:1 ratio required for the formation of the ferrite phase MFe_2O_4 (where M = Ni or Zn). As a result, only a fraction of the metal ions can participate in the formation of the spinel Ni(Zn)Fe_2O_4 phase. The excess Zn^{2+} and Ni^{2+} ions that are not incorporated into the spinel lattice subsequently crystallize into ZnO and β-Ni(OH)$_2$ phases, respectively. These findings demonstrate that the initial precursor molar ratio has a strong influence on phase distribution and the phase purity of the final products obtained after the hydrothermal reaction.

The phase fractions, lattice parameters, crystallite sizes, and microstrain of the different phases in the R series samples were determined from Rietveld refinement and are summarized in Table 2. Under identical synthesis conditions, the lattice parameters exhibit only minor variations, indicating the structural stability of each phase after synthesis. For the $NiFe_2O_4$ phase, the lattice parameter *a* of the pure NFO sample is 8.341 Å.

Table 2. The phase fractions, lattice parameters, crystallite sizes (*D*), and microstrain (*ε*) of the different phases in the M series samples.

Sample	χ^2	Rwp	Phase	Content (%)	Lattice parameter (Å)	*D* (nm)	*ε* (%)

NFO	1.23	8.9	$NiFe_2O_4$	100	*a*= 8.341	17.40	0.13
ZnO	1.27	9.2	ZnO	100	*a*= 3.249 *c*= 5.206	26.74	0.23
M-1	1.47	16.3	$Ni(Zn)Fe_2O_4$	80.79	*a*= 8.458	21.39	0.25
			β-$Ni(OH)_2$	11.01	*a*= 3.130 *c*= 4.616	11.45	1.34
			ZnO	6.25	*a*= 3.257 *c*= 5.212	29.18	0.21
			α-Fe_2O_3	1.95	-	-	0.33
M-1,5	1.35	14.8	$Ni(Zn)Fe_2O_4$	42.46	*a*= 8.473	22.75	0.21
			β-$Ni(OH)_2$	8.06	*a*= 3.126 *c*= 4.619	12.82	1.66
			ZnO	46.86	*a*= 3.256 *c*= 5.213	29.08	0.15
			α-Fe_2O_3	2.62	-	-	0.06
M-2	1.83	17.2	$NiFe_2O_4$	32.68	*a*= 8.482	24.76	0.29
			β-$Ni(OH)_2$	7.78	*a*=3.132 *c*= 4.615	12.07	1.19
			ZnO	57.2	*a*= 3.258 *c*= 5.215	29.97	0.12
			α-Fe_2O_3	0.34	-	-	0.41

For the spinel $Ni(Zn)Fe_2O_4$ phase, the lattice parameter *a* increases from 8.458 Å for the M-1 sample to 8.473 Å for M-1,5 and reaches 8.482 Å for M-2. This gradual increase indicates the progressive substitution of Zn^{2+} ions with a larger ionic radius (0.74 Å) into the spinel lattice in place of Ni^{2+} ions with a smaller ionic radius (0.69 Å), leading to lattice expansion. This behavior is consistent with the increasing Zn content introduced through the initial precursors. Figure 3 presents the XRD patterns of the M-series samples in the 2θ range of 34°–37°. With increasing Zn^{2+} ion ratio, the intensity of the ZnO (101) diffraction peak increases relative to the (311) peak of the $Ni(Zn)Fe_2O_4$ phase. No peak shift is observed for the ZnO (002) and (101) reflections; however, the (311) reflection of the $Ni(Zn)Fe_2O_4$ phase exhibits a noticeable shift toward lower diffraction angles.

The nearly constant lattice parameters of the ZnO and β-$Ni(OH)_2$ phases indicate their structural stability during the synthesis process. The calculated crystallite size and lattice strain of the M-1, M-1,5, and M-2 samples reveal that the crystallite size of the spinel $Ni(Zn)Fe_2O_4$ phase increases from D = 21.39 nm for M-1 to 22.75 nm for M-1,5 and 24.76 nm for M-2, suggesting that crystal growth is promoted when larger Zn^{2+} ions substitute smaller Ni^{2+} ions. In contrast, the crystallite sizes of the ZnO and β-$Ni(OH)_2$ phases show no significant variation.

Figure 4 presents the SEM micrographs of the NFO, ZnO, M-1,5 and M-2 samples. The NFO sample consists of fine nanoparticles in the range of 20–30 nm, some of which have agglomerated during the hydrothermal process to form polyhedral (octahedral-like) structures with an average size of approximately 200 nm, a typical morphology for hydrothermally synthesized $NiFe_2O_4$. The ZnO sample displays uniformly distributed nanoparticles with sizes between 40 and 60 nm. Both the M-1,5 and M-2 samples exhibit small particles that are agglomerated, with no well-defined particle morphology.

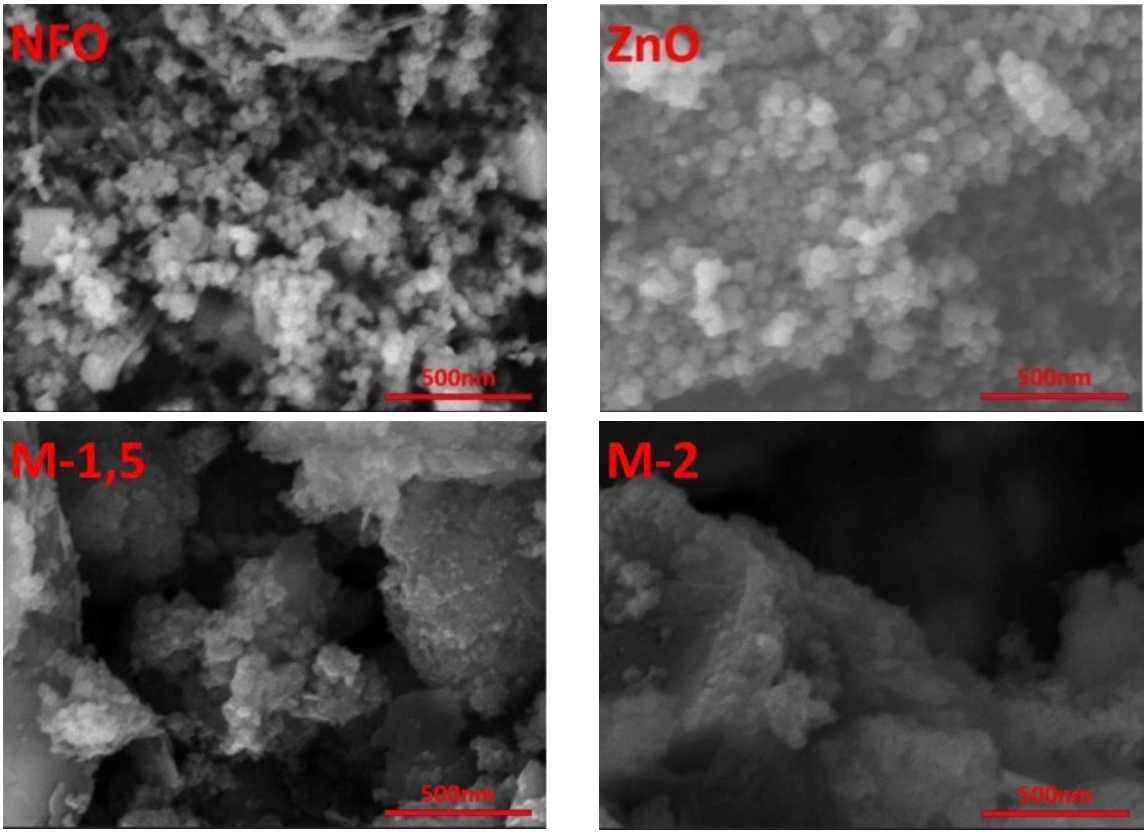

Figure 4. SEM images of the NFO, ZnO, M-1,5, and M-2 samples.

3.2. Magnetic Properties

The magnetic properties of the samples was examined at room temperature using hysteresis loop measurements obtained with a vibrating sample magnetometer (VSM) under an applied magnetic field ranging from –15,000 Oe to +15,000 Oe. Figure 5 displays the hysteresis loops of NFO, ZnO, R-1, R-1,5, and R-2, while the corresponding coercivity *Hc* and saturation magnetization *Ms* values are summarized in Table 3.

The results confirm that ZnO exhibits no magnetic properties (*Ms* = 0 emu/g, *Hc* = 0 Oe) due to the $3d^{10}$ electronic configuration of Zn^{2+}. In contrast, $NiFe_2O_4$ ferrite shows soft magnetic behavior with *Ms* = 41.9 emu/g and *Hc* = 29.5 Oe, consistent with its inverse spinel structure. The saturation magnetization *Ms* values of the M-1, M-1,5, and M-2 samples are 9.7 emu/g, 7.0 emu/g, and 5.4 emu/g, respectively, while the corresponding coercivity *Hc* values are 12.6 Oe, 13.2 Oe, and 13.9 Oe. The M-1,5 sample exhibits *Ms* and *Hc* values comparable to those reported by A. Manikandan et al. for $Zn_{0.7}Ni_{0.3}Fe_2O_4$, which showed *Ms* = 7.4 emu/g and *Hc* = 9.1 Oe [8]. The decrease in saturation magnetization with increasing Zn^{2+}/Ni^{2+} ratio can be attributed to two main factors. First, increasing the Zn^{2+} content modifies the spinel structure of $Ni(Zn)Fe_2O_4$, as Zn^{2+} ions preferentially occupy the tetrahedral (A) sites and are non-magnetic, whereas Ni^{2+} and Fe^{3+} ions are distributed over both tetrahedral (A) and octahedral (B) sites, giving rise to ferrimagnetic A–B superexchange interactions. Substitution of Ni^{2+} by Zn^{2+} reduces the density of Fe^{3+}(A)–O^{2-}–Fe^{3+}(B) and/or Ni^{2+}(B)–O^{2-}–Fe^{3+}(A) superexchange pathways, leading to a reduction in magnetization [9]. Second, at higher Zn^{2+} ratios, the increased formation of

non-magnetic secondary phases such as ZnO and β-$Ni(OH)_2$, as revealed by structural analysis, further decreases the overall magnetization of the material.

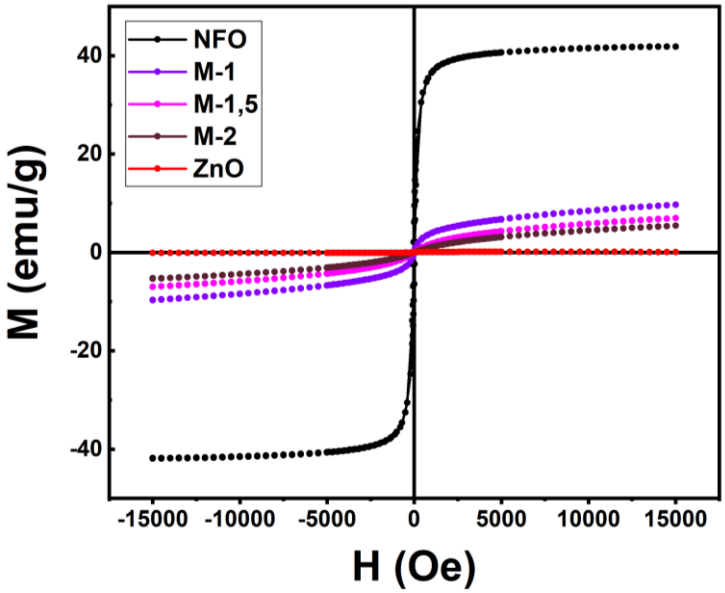

Figure 5. Hysteresis curves of the M series samples.

However, the coercivity *Hc* of this sample series shows a slight increasing trend with increasing Zn^{2+} ion content. This behavior can be attributed to the effects of crystal defects, internal stress, and, in particular, the formation of a higher density of heterointerfaces between different phases, such as Ni(Zn)Fe_2O_4–ZnO and Ni(Zn)Fe_2O_4–β-$Ni(OH)_2$. These interfacial regions induce domain wall pinning effects, hindering domain wall motion under an applied magnetic field and thereby leading to an increase in *Hc* [10]. In addition, spin canting at the phase boundaries also contributes to the enhancement of coercivity and the reduction of Ms.

Table 3. Coercivity (*Hc*) and Saturation Magnetization (*Ms*) of the M series Samples.

Sample	NFO	ZnO	M-1	M-1,5	M-2
Hc	29.5	0	12.6	13.2	13.9
Ms	41.9	0	9.7	7.0	5.4

3.3. Optical Properties

The optical properties of the materials were examined using UV–Vis reflectance spectra, as shown in Figure 6 for NFO, ZnO, M-1, M-1,5, and M-2. The pure ZnO sample exhibits a sharp absorption edge near 380 nm, with reflectance dropping to nearly zero at shorter wavelengths. At longer wavelengths, the reflectance gradually increases, primarily due to particle scattering. In contrast, NFO shows very low reflectance (<5%) across a broad wavelength range of 250–550 nm, followed by a gradual increase beyond 550 nm. The reflectance spectra of the M-1, M-1,5, and M-2 samples exhibit a minimum reflectance intensity in the wavelength range of 350–380 nm. At wavelengths above 380 nm, the reflectance intensity begins to increase. Over the entire spectral range from 250 to 800 nm, the M-2 sample, which contains the highest Zn^{2+} ratio, shows the highest reflectance, whereas the lowest

reflectance is observed for the M-1 sample with the lowest Zn^{2+} content. Since ZnO possesses a larger band gap energy (Eg), it strongly absorbs in the ultraviolet region while exhibiting high reflectance in the visible region, thereby contributing to the increased reflectance of the samples under visible light. Conversely, increasing the ZnO content reduces the fraction of the Ni(Zn)Fe_2O_4 phase, which is the primary component responsible for photon absorption in the visible region; as a result, the optical absorption capability in this spectral range is significantly diminished.

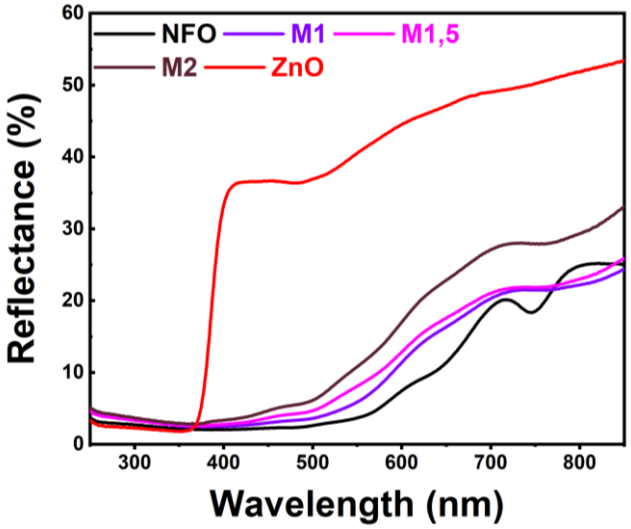

Figure 6. Reflectance spectra of the M series samples.

The band gap energy of the ZnO sample was determined to be *Eg* = 3.28 eV, while that of the NFO sample was *Eg* = 1.61 eV. The optical band gap energies of the M-series samples (M-1, M-1,5, and M-2) were determined to be 2.12 eV for M-1, 2.08 eV for M-1,5, and 2.08 eV for M-2, respectively. The obtained *Eg* values for the M-series samples are in good agreement with the results reported by A. Manikandan et al. for $Zn_{0.9}Ni_{0.1}Fe_2O_4$ and $Zn_{0.8}Ni_{0.2}Fe_2O_4$, which exhibited band gap energies of 2.1 eV and 2.07 eV, respectively [8]. The negligible variation among the *Eg* values indicates that the optical band gap of the entire material system is predominantly governed by the Ni(Zn)Fe_2O_4 phase formed during the synthesis process.

Table 4. Zn^{2+}/Ni^{2+} ratios of the M series samples.

Sample	NFO	ZnO	M-1	M-1,5	M-2
Eg	1.61	3.28	2.12	2.08	2.08

4. Conclusion

In this study, ZnO/$NiFe_2O_4$ nanocomposites were successfully synthesized via a hydrothermal route. The pure $NiFe_2O_4$ sample exhibited spherical and octahedral morphologies with average particle sizes of approximately 20–30 nm and ~200 nm, respectively. It demonstrated soft magnetic characteristics with a saturation magnetization of 41.9 emu/g, a coercivity of 29.5 Oe, and a band gap energy of 1.61 eV. In contrast, pure ZnO consisted of non-magnetic particles sized 40–60 nm and exhibited a band gap of 3.28 eV. For the composite samples, optical absorption was extended from the UV to the visible

region (250–800) nm. The estimated band gap values of the composites were in the range of 2.08–2.12 eV, dominated by the narrower-gap $NiFe_2O_4$ phase. The obtained optical absorption in the visible region and the magnetic recoverability indicate that the $ZnO/NiFe_2O_4$ composites possess potential for future application as magnetically separable photocatalysts. However, detailed photocatalytic performance evaluation will be investigated in subsequent studies.

Acknowledgments

This work was carried out with the support of the NAFOSTED project under grant number 103.02-2023.60.

References

[1] A. Mills, S. L. Hunte, An Overview of Semiconductor Photocatalysis, J. Photochem. Photobiol., Vol. 12, No. 296, 1997, pp. 346-347, https//doi.org/10.1126/science.12.296.346-a.

[2] Z. Mirzaeifard, Z. Shariatinia, M. Jourshabani, S. M. Rezaei Darvishi, ZnO Photocatalyst Revisited: Effective Photocatalytic Degradation of Emerging Contaminants Using S-Doped ZnO Nanoparticles under Visible Light Radiation, Ind. Eng. Chem. Res., Vol. 59, No. 36, 2020, pp. 15894-15911. https//doi.org/10.1021/acs.iecr.0c03192.

[3] K. Mondal, A. Sharma, Recent Advances in the Synthesis and Application of Photocatalytic Metal-metal Oxide Core-shell Nanoparticles for Environmental Remediation and Their Recycling Process, RSC Adv., Vol. 6, No. 87, 2016, pp. 83589-83612, https//doi.org/10.1039/c6ra18102c.

[4] M. A. Hassaan, A. Pantaleo, F. Santoro, M. R. Elkatory, G. D. Mastro, A. E. Sikaily, S. Ragab, A. E. Nemr, Techno-economic Analysis of ZnO Nanoparticles Pretreatments for Biogas Production from Barley Straw, Energies, Vol. 13, No. 18, 2020, https//doi.org/10.3390/en13195001.

[5] M. A. Hassaan, M. A. E. Nemr, M. R. Elkatory, S. Ragab, V. C. Niculescu, A. E. Nemr, Principles of Photocatalysts and Their Different Applications: A Review, Springer International Publishing, Vol. 381, No. 6. 2023, https//doi.org/10.1007/s41061-023-00444-7.

[6] Ü. Morkoc, H. Özgür, Wide Bandgap Light Emitting Materials and Devices Liquid Phase Epitaxy of Electronic, Optical and Optoelectronic Materials, 2009.

[7] K. Choi, T. Kang, S. G. Oh, Preparation of Disk Shaped ZnO Particles Using Surfactant and their PL Properties, Mater. Lett., Vol. 75, pp. 240-243, 2012, https//doi.org/10.1016/j.matlet.2012.02.031.

[8] A. Manikandan, J. J. Vijaya, L. J. Kennedy, Comparative Study of Pure and Ni-doped ZnFe2O4 Nanoparticles for Structural, Optical and Magnetic Properties, Adv. Mater. Res., vol. 699, 2013, pp. 524-529, https//doi.org/10.4028/www.scientific.net/AMR.699.524.

[9] S. Mitra, K. Mandal, P. Anil Kumar, Temperature Dependence of Magnetic Properties of NiFe2O4 Nanoparticles Embeded in SiO2 Matrix, J. Magn. Magn. Mater., Vol. 306, No. 2, 2006, pp. 254-259, https//doi.org/10.1016/j.jmmm.2006.03.024.

[10] J. C. Maurya, P. S. Janrao, A. A. Datar, N. S. Kanhe, S. V. Bhoraskar, V. L. Mathe, Evidence of Domain Wall Pinning in Aluminum Substituted Cobalt Ferrites, J. Magn. Magn. Mater., Vol. 412, 2016, pp. 164-171, https//doi.org/10.1016/j.jmmm.2016.03.074.